



JES FOCUS ISSUE ON MECHANO-ELECTRO-CHEMICAL COUPLING IN ENERGY RELATED MATERIALS AND DEVICES

Structural Evolution and Pulverization of Tin Nanoparticles during Lithiation-Delithiation Cycling

Jiangwei Wang,^a Feifei Fan,^b Yang Liu,^c Katherine L. Jungjohann,^c Seung Woo Lee,^b Scott X. Mao,^{a,z} Xiaohua Liu,^{c,z} and Ting Zhu^{b,*}

^aDepartment of Mechanical Engineering and Materials Science, University of Pittsburgh, Pittsburgh, Pennsylvania 15261, USA

^bWoodruff School of Mechanical Engineering, Georgia Institute of Technology, Atlanta, Georgia 30332, USA

^cCenter for Integrated Nanotechnologies, Sandia National Laboratories, Albuquerque, New Mexico 87185, USA

Pulverization is a major cause of the capacity fade and poor cyclability of Sn-based anodes in lithium-ion batteries. We study the structural evolution of Sn nanoparticles during electrochemical lithiation-delithiation cycling by in situ transmission electron microscopy (TEM). The β -Sn nanoparticles in the size range of 79–526 nm are lithiated to the crystal $\text{Li}_{22}\text{Sn}_5$ phase via a two-step mechanism, and no cracking or fracture is observed, distinct from the lithiation-induced fracture in micron-sized Sn particles. Lithiation can induce the aggregation of small Sn nanoparticles with diameter in tens of nanometers, while delithiation can lead to the pulverization of large Sn nanoparticles. Similarly, the aggregation and pulverization of Sn nanoparticles are also observed during sodiation and desodiation, respectively. The delithiation/desodiation induced pulverization of Sn nanoparticles is attributed to the high dealloying rate that results in cracks and voids in dealloyed Sn anodes. Based on our in situ TEM results, a size-dependent pulverization mechanism of Sn particles is proposed. Our work advances the mechanistic understanding of the pulverization and degradation mechanisms of Sn particle-based electrodes in Li-ion batteries.

© 2014 The Electrochemical Society. [DOI: 10.1149/2.0041411jes] All rights reserved.

Manuscript submitted June 17, 2014; revised manuscript received August 6, 2014. Published August 15, 2014. This was Paper 324 presented at the Orlando, Florida, Meeting of the Society, May 11–15, 2014. *This paper is part of the JES Focus Issue on Mechano-Electro-Chemical Coupling in Energy Related Materials and Devices.*

Advanced Li-ion batteries (LIBs) for next-generation electric vehicles and portable electronics require new electrode materials with low cost, high capacity and superior cyclability.^{1–4} Tin (Sn) is a promising candidate anode material with high capacities.^{5,6} The theoretical capacity of the Sn anode is 994 mAh/g,⁵ which is about three times that of the commercialized graphite anode (372 mAh/g)⁵ in current LIBs. Sn is also nontoxic, inexpensive and naturally abundant. Hence the Sn-based anode materials have attracted significant attention in the past few years.^{2–12} The electrochemical performance of Sn anodes can be improved greatly by reducing the particle size to nanoscale or using Sn/C-based nanocomposites.^{7–12} However, one critical problem is the drastic structural changes of Sn particles through their pulverization^{11,13,14} and aggregation^{15–18} during charge-discharge cycling. These changes usually result in electrically disconnected particles and consume active Li ions to form new solid electrolyte interphases (SEIs), leading to capacity fade.^{6,7,19,20} To mitigate the electrode degradation, it is important to understand the mechanism of structural evolution of Sn particles through correlation with their sizes and cycle responses.

Considerable efforts have been devoted to study the pulverization and capacity fade of Sn anodes in the past few years. Ex situ experiments showed the pulverization of Sn-based anodes after electrochemical cycles.^{14,21} Although pulverization is generally attributed to the large and inhomogeneous volume changes during Li insertion and extraction,^{14,22–24} its detailed mechanism remains unclear. Recently, in situ experiments have been conducted to observe the structural changes of Sn particles in lithiation-delithiation^{20,25} and sodiation-desodiation²⁶ cycles. In micron-sized Sn particles, pulverization was observed and attributed to the cracks generated by the lithiation-induced large volume expansion (258%).^{20,25} On the other hand, for small nanoparticles (NPs, e.g. ~10 nm in diameter), aggregation often occurs, leading to formation of larger NPs that pulverize in subsequent cycles.^{11,15–18} However, the mechanism of aggregation is unclear. These differences in experiments also suggest that the pulverization of Sn particles may involve a size-dependent mechanism.

In this work, the electrochemical lithiation and delithiation of Sn NPs are studied by in situ transmission electron microscopy (TEM).

We observe a two-step lithiation mechanism without cracking or fracture in Sn NPs with a wide size range of 79–526 nm. In addition, we find that small Sn NPs can fuse together during lithiation. Also, small NPs are frequently generated from the mother NPs during delithiation, leading to pulverization. Similar pulverization processes are also observed during sodiation-desodiation cycling. Based on in situ observations, a size-dependent pulverization mechanism of Sn particles is proposed, shedding light onto how the Sn particle-based electrodes degrade in Li-ion and Na-ion batteries.

Experiments and Results

Figure 1a shows a schematic of the nanoscale battery setup in TEM. The Sn NPs with different diameters (purchased from Skyspring Nanomaterials Inc.) are single crystals with a tetragonal lattice structure (β -Sn), as shown in our recent work.²⁶ They are dispersed on a platinum (Pt) rod to serve as the working electrode. The bulk Li metal on a tungsten (W) rod is used as the counter electrode, and the native Li_2O on the Li surface acts as the solid electrolyte. This all-solid setup enables a real-time observation of the structural evolution in individual NP electrodes during electrochemical cycling.^{26–30} The experiments are conducted under either the electron beam-on condition with a low current density or the beam-blank condition, so as to reduce the beam effect on the lithiation-delithiation processes. A negative potential of -1 V is applied against the Li electrode to initiate the lithiation. Figure 1b–1h shows the typical structural changes of Sn NPs during the first lithiation. The lithiation of Sn NPs is dominated by a two-step mechanism, similar to the sodiation of Sn NPs.²⁶ That is, Sn NPs are initially lithiated with a limited volume expansion, yielding a Li-poor amorphous Li_xSn (a - Li_xSn) phase (Figure 1b–1e); then they are further lithiated with a much larger volume expansion, resulting in the final product of a Li-rich crystalline $\text{Li}_{22}\text{Sn}_5$ (c - $\text{Li}_{22}\text{Sn}_5$) phase (Figure 1e–1h). More specifically, in the first step of lithiation, a phase boundary is clearly visible to separate the lithiated and unlithiated regions, suggesting a two-phase mechanism involved. Incidentally, a sharp phase boundary was also observed during the lithiation and sodiation of other systems, such as Li-Si^{27,29} and Na-Sn.²⁶ As the phase boundary migrates (indicated by the yellow arrows in Figure 1c–1d), pristine Sn is consumed, forming a new a - Li_xSn phase. After the phase boundary sweeps through the entire Sn NP, the volume expansion only

*Electrochemical Society Active Member.

^zE-mail: ting.zhu@me.gatech.edu; lxhua99@gmail.com; sxm2@pitt.edu

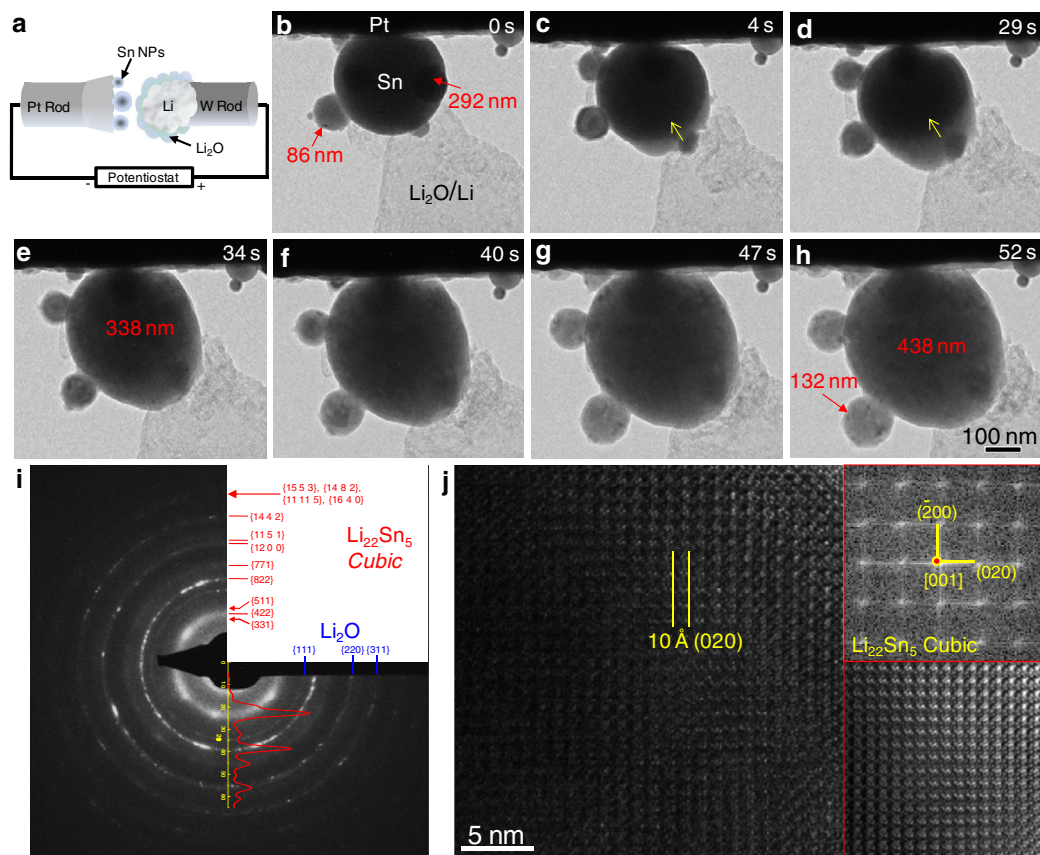


Figure 1. In situ TEM of Sn NPs during the first lithiation. (a) Schematic of a nanoscale Li-ion battery in TEM. (b-h) Time-lapse TEM images of electrochemical lithiation of individual Sn NPs. The pristine Sn NPs are in the spherical shape with different diameters. The lithiation of Sn NPs involves a two-step mechanism. Namely, in (b-e), the NPs are initially lithiated by a two-phase mechanism through the propagation of a sharp phase boundary (indicated by the yellow arrows) between the pristine Sn and a Li-poor amorphous Li_xSn ($a\text{-Li}_x\text{Sn}$) phase; then in (f-h), the NPs are further lithiated without a visible phase boundary, yielding the final $c\text{-Li}_{22}\text{Sn}_5$ phase. (i) The electron diffraction pattern (EDP) after full lithiation. The fully lithiated phase is identified as $c\text{-Li}_{22}\text{Sn}_5$ with a cubic structure. The inserted curve is the simulated powder diffraction of the $c\text{-Li}_{22}\text{Sn}_5$ phase, which agrees well with the measured EDP. (j) High resolution TEM (HRTEM) image, fast Fourier transform (FFT) pattern and inverse FFT (IFFT) image of the product $c\text{-Li}_{22}\text{Sn}_5$ phase. The HRTEM image is taken from another sample.

reaches $\sim 55\%$, indicating a relatively low Li content in the resultant $a\text{-Li}_x\text{Sn}$ phase. In the second step of lithiation, the $a\text{-Li}_x\text{Sn}$ phase is further lithiated without an observable phase boundary. The final product after full lithiation is $c\text{-Li}_{22}\text{Sn}_5$, giving a total volume expansion of $\sim 239\%$ relative to pristine Sn. Figure 1i shows the electron diffraction pattern (EDP) after full lithiation, which is identified as the $c\text{-Li}_{22}\text{Sn}_5$ phase with a cubic structure. The inserted curve in Figure 1i is the simulated powder diffraction of $c\text{-Li}_{22}\text{Sn}_5$ ($a = 19.78 \text{ \AA}$, space group 196),³¹ in agreement with the EDP of $c\text{-Li}_{22}\text{Sn}_5$ from experiment. Figure 1j presents the high resolution TEM (HRTEM) image, fast Fourier transform (FFT) pattern and inverse FFT (IFFT) image of the $c\text{-Li}_{22}\text{Sn}_5$ phase. The measured lattice spacing of (020) planes in $c\text{-Li}_{22}\text{Sn}_5$ is approximately 10 \AA , close to the theoretical value of 9.9 \AA . This result further confirms the product phase of $c\text{-Li}_{22}\text{Sn}_5$ after full lithiation.

Next we analyze the Li content in $a\text{-Li}_x\text{Sn}$ after the first step of lithiation. Multiple Li-Sn alloy phases exist in the binary Li-Sn phase diagram.³² Due to the similar diffraction patterns of several intermediate Li-Sn phases,³³ it is difficult to determine the x value in $a\text{-Li}_x\text{Sn}$ by comparing EDPs of $a\text{-Li}_x\text{Sn}$ and Li-Sn alloys. Therefore, we only estimate the Li content in $a\text{-Li}_x\text{Sn}$ based on volume expansions.^{1,26} Table I lists the measured volume expansions of several Sn NPs with different initial diameters after the first step of lithiation, along with their expansions after full lithiation. Table II presents the theoretical values of volume expansion for different Li_xSn alloy phases, which closely follow a linear relationship with Li content (Figure 2). The measured volume expansions after the first step of lithiation are in

Table I. Measured volume expansions after the first step of lithiation and the full lithiation.

	Pristine NP sizes (nm)	1st-step lithiation	Full lithiation
Volume expansion	86	63%	261%
	156	50%	249%
	292	55%	239%
	132		267%
	291		242%
	350		271%
	423		255%

between 50–63%, close to the theoretical value of the LiSn phase (52%). Previous studies showed that the Li_2Sn_5 phase formed after the initial lithiation.^{24,34} The discrepancy between the present study and the earlier tests^{24,34} might be caused by different experimental setups, sample conditions and lithiation rates, which could affect the reaction kinetics and accordingly product phase.²⁶ After full lithiation to the $c\text{-Li}_{22}\text{Sn}_5$ phase, the measured volume expansions in our experiments are in the range of 239–271%, close to the theoretical value of 258% for $c\text{-Li}_{22}\text{Sn}_5$.

Figure 3 and Figure 4 present additional in situ TEM results on lithiation of Sn NPs with different sizes. Figure 4a–4c shows a typical core-shell structure observed during the first step of lithiation, which

Table II. Theoretical values of volume expansion for different Li_xSn phases.

Phase ^a	Li_2Sn_5	LiSn	Li_7Sn_3	Li_5Sn_2	$\text{Li}_{13}\text{Sn}_5$	Li_7Sn_2	$\text{Li}_{22}\text{Sn}_5$
Volume expansion ^b	22%	52%	126%	138%	142%	197%	258%

^aThe different Li-Sn crystal phases are based on the ICSD.³¹

^bThe theoretical volume expansions of different Li_xSn phases are calculated based on the following methods. The unit cell of $\beta\text{-Sn}$ contains four Sn atoms, while the unit cell of Li_xSn phases contain n Sn atoms. The theoretical volume expansions are estimated according to:

$$\text{Volume expansion} = \left(\frac{V_{\text{Li}_x\text{Sn}}}{V_{\text{Sn}} \times \frac{x}{4}} - 1 \right) \times 100\%$$

where, $V_{\text{Li}_x\text{Sn}}$ and V_{Sn} are the volume of the unit cell of Li_xSn and $\beta\text{-Sn}$, respectively.

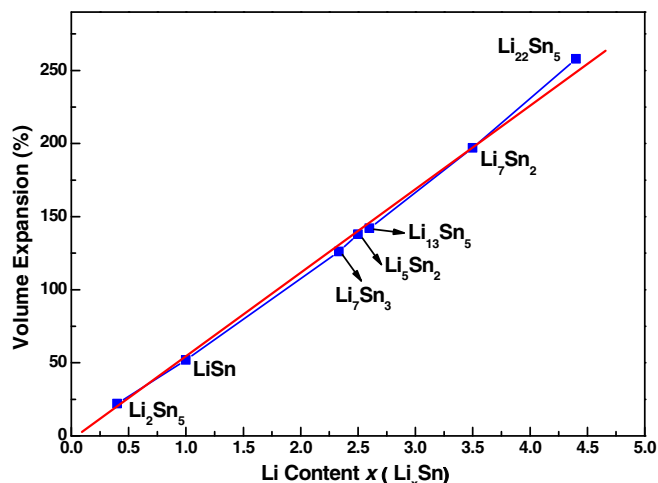


Figure 2. The linear relationship between the theoretical volume expansion and the Li content for different Li_xSn alloy phases. The blue line connects the calculation data points (squares), and the red line represents the linear fitting result.

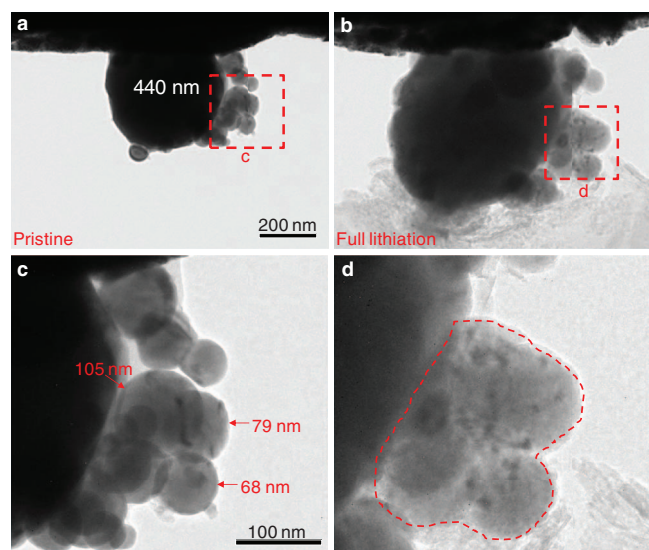


Figure 3. Lithiation of a large Sn NP without fracture and aggregation of smaller Sn NPs during lithiation. (a) A large Sn NP with the initial diameter of 440 nm and adjacent small NPs before lithiation. (b) After full lithiation under the beam-blank condition, no cracking or fracture is observed in all NPs. (c) A zoom-in image before lithiation, showing a cluster of three separated small pristine Sn NPs with the diameter of 105 nm, 79 nm and 68 nm, respectively. (d) A zoom-in image after lithiation, showing that the three small NPs are fused together to form a large $c\text{-Li}_{22}\text{Sn}_5$ NP.

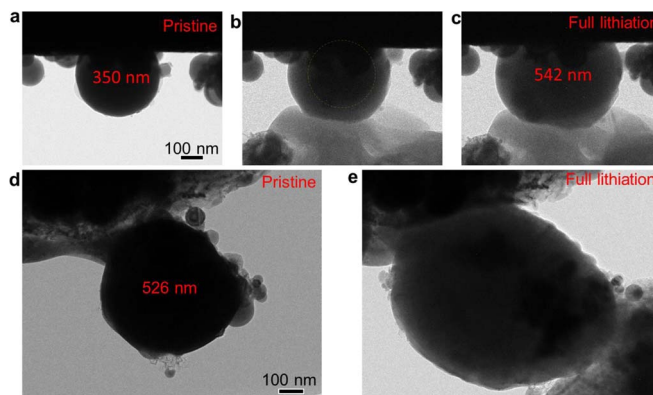


Figure 4. Lithiation of large Sn NPs without cracking. (a-c) Lithiation of a Sn NP with the initial diameter of 350 nm. A core-shell structure forms during lithiation. (d-e) Lithiation of a Sn NP with the initial diameter of 526 nm. No cracking or fracture is observed in both cases after full lithiation.

confirms the active two-phase mechanism as discussed above and, more importantly, the faster diffusion of Li ions on the surface than in the bulk. The spherical core-shell structure also indicates the isotropic lithiation of Sn particles; namely, the mobility of the two-phase boundary (i.e., the core-shell interface) is insensitive to its crystallographic orientation.^{35,36} Notably, we have tested more than thirty Sn NPs with a size range of 79–526 nm, and no cracking or fracture is observed after full lithiation to $c\text{-Li}_{22}\text{Sn}_5$ under both beam-blank and weak-beam conditions. The tough behavior of Sn NPs revealed from our in situ TEM experiments is in contrast with the lithiation response of micron-sized Sn particles where cracks were frequently observed by in situ X-ray transmission microscopy.^{20,25} To understand such different fracture behaviors, we note that recent in situ TEM experiments have demonstrated the size-dependent fracture during the lithiation of crystalline Si NPs.³⁰ Fracture in large Si NPs was attributed to the strong lithiation anisotropy (i.e., the orientation dependence of the core-shell interface mobility), which results in a large, nonuniform tensile hoop stress in the surface layer of Si NPs for driving the surface cracking.³⁷ Below the critical size of ~ 150 nm, the driving force of crack extension becomes too small to fracture the lithiated Si NPs.³⁰ On the other hand, recent in situ TEM experiments also showed that the crystalline Ge NPs exhibited tough behaviors due to their weak lithiation anisotropy despite the similar volume expansion as Si, and no cracking or fracture was observed after full lithiation in crystalline Ge NPs as large as 620 nm.³⁸ Hence, we attribute the tough lithiation behaviors of Sn NPs to the following factors. First, the isotropic lithiation of Sn NPs leads to a uniform hoop tension, similar to Ge NPs.³⁸ Second, Sn NPs show a unique two-step lithiation, and the two-phase lithiation appears to occur only in the first step of lithiation. As a result, the volume expansion in the initial lithiation is much smaller than that after full lithiation, thereby resulting in the smaller hoop stress in the surface layer of lithiated Sn NPs. Third, Sn and Li_xSn alloys are expected to have a relatively low yield strength and good ductility compared to Si counterparts at room temperature, considering that the melting point of Sn (232°C) is much lower than that of Si (1414°C). However, as the size of Sn particles increases to

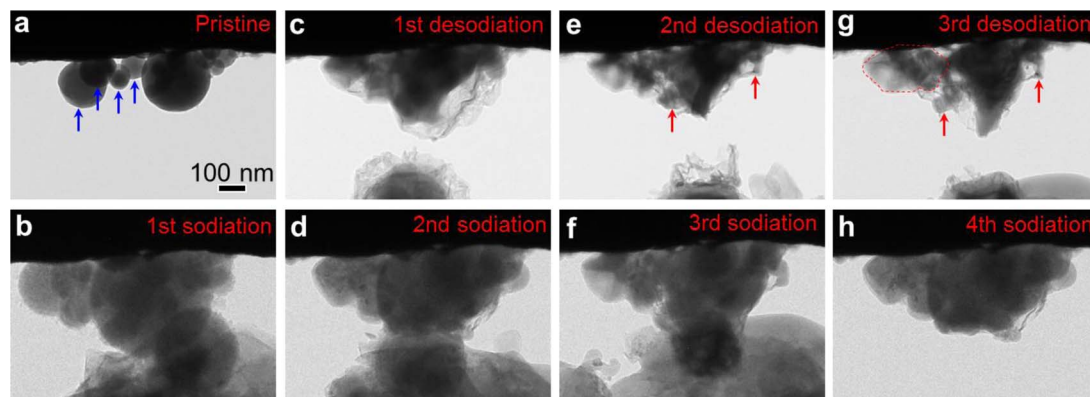


Figure 5. Structural evolution of Sn NPs during sodiation-desodiation cycling. (a-c) Sodiation causes aggregation of smaller Sn NPs, which yields a single Sn NP larger than its parent NPs during the subsequent desodiation. (e, g) Desodiation could induce pulverization of large Sn NPs. That is, the new small Sn NPs are generated after several sodiation-desodiation cycles. The blue arrows indicate several individual Sn NPs before sodiation-desodiation cycles, while the red arrows indicate the new small Sn NPs formed during desodiation.

several micrometers, the lithiation-induced hoop stress and accordingly the driving force of crack extension could become sufficiently large to fracture the micron-sized particles from the lithiated surface layer.

Interestingly, the fusions of small Sn NPs are often observed during in situ TEM experiments of lithiation. Figure 3c shows three neighboring Sn NPs with the diameter of 105 nm, 79 nm and 68 nm, respectively. After lithiation, they are fused to form a single large NP of $c\text{-Li}_{22}\text{Sn}_5$. Such kind of fusion has been previously observed during the lithiation of Si nanowires and NPs,^{39,40} which were attributed to the lithiation-induced material flow and surface welding.⁴⁰ Subsequent dealloying (e.g., desodiation) yields a single Sn NP larger than its parent NPs (Figure 5). While previous ex situ observations have showed aggregation of Sn-based NPs after charge-discharge cycles,¹⁵⁻¹⁷ the mechanism of aggregation remains unclear. Our in situ TEM directly reveals that the fusion of Sn NPs can occur during the initial lithiation/sodiation. The resultant large alloy particles can undergo further morphological changes and even pulverize during subsequent cycling (Figure 5).

Figure 6a-6c presents the TEM images of a pair of Sn NPs in the first lithiation-delithiation cycle. The experiment is conducted under the beam-blank condition. Of particular note are the morphological changes occurring during the delithiation. The spherical Sn NPs are transformed into irregular shapes after one cycle, and smaller Sn NPs (~20 nm in diameter) appear near the mother NPs after full delithiation, as indicated by red arrows in Figure 6c. Similar morphological changes are also observed in Sn NPs after sodiation-desodiation cycles (Figure 5). This provides a direct evidence of pulverization occurring during the dealloying process. Such delithiation/desodiation-induced morphological changes arise possibly owing to the high dealloying rate associated with the applied large voltage load in Sn, Li-Sn and Na-Sn alloys. This could induce a large concentration gradient and thus a high stress/strain in the dealloyed Sn region. The high stress/strain can lead to cracking and facilitate void formation in dealloyed Sn anodes,⁴¹ resulting in the production of smaller daughter NPs. Figure 6d-6g shows another in situ TEM result of the delithiation process. In this case, the lithiation-induced surface oxide layer forms a stable shell (Figure 6d), which effectively serves as the SEI layer. After delithiation, the surface SEI shell exhibits negligible shrinkage, and a large void forms inside the shell (Figure 6f-6g). This void accommodates the volume loss (*i.e.*, the production of free volumes) associated with the extraction of Li ions, thereby reducing the overall volume change of the Sn NP after delithiation. The dealloying-induced voids have also been observed in the delithiation/desodiation of Sn particles with different sizes (from several micrometers to hundreds of nanometers).^{25,26} Such dealloying-induced voids are presumably caused by the vacancy-mediated diffusion, while the specific dealloying morphologies are controlled by the particle size, Li content and

dealloying rate, etc.⁴² In addition, some small individual Sn NPs can be generated on the SEI shell after full delithiation (indicated by the red arrows and inset in Figure 6g). However, those NPs can be further lithiated due to their connections with the surface Li source. As a result, the capacity fade could be effectively reduced. Similar behaviors are also observed during the sodiation-desodiation cycling (Figure 5).

After full delithiation, NPs are transformed back to the crystalline Sn with a tetragonal structure ($\beta\text{-Sn}$), as shown by both the EDP and HRTEM image (Figure 6h-6i). This is consistent with the phase transformation of cycled Sn anodes reported in the literature.^{13,18,20,24} However, in a recent study of Sn NPs (~10 nm in diameter) by Xu et al.,³³ $\alpha\text{-Sn}$ with a cubic structure was obtained after delithiation, in contrast to $\beta\text{-Sn}$ in the present and previous studies.^{13,15-18,20,24,26} It is well known that $\alpha\text{-Sn}$ is a semiconductor with low conductivity; it is brittle, powdery, and only stable under low temperature (< 13.2 °C).⁴³ Moreover, the phase transformation from $\beta\text{-Sn}$ to $\alpha\text{-Sn}$ can result in Sn and Sn-based alloys crumbled into powders (referred to as the so-called tin pest or tin disease, *i.e.*, pulverization),^{43,44} leading to the well-known failure of "Napoleon's buttons".⁴⁴ Therefore, the drastic mechanical damage and pulverization of Sn NPs observed by Xu et al.³³ could probably be related to the formation of brittle $\alpha\text{-Sn}$. However, it remains unclear regarding the key factors governing the formation of $\alpha\text{-Sn}$, such as electrochemical load, temperature and particle size.

Discussion

Based on the above in situ studies of Sn NPs and in conjunction with the earlier results of Sn microparticles,^{20,25,26} we summarize, in Figure 7, a size-dependent pulverization mechanism of Sn particles upon electrochemical cycling. In Sn microparticles, cracking and fracture occur during lithiation due to the high stress generated by the large, non-uniform volume expansion.^{20,22,25} Repeated fractures subdivide the particles, causing the pulverization of electrodes during cycling (Figure 7a). In contrast, in Sn NPs, the volume expansion occurring during lithiation can be effectively accommodated without fracture (Figure 7b). This can be attributed to the small particle size and the unique two-step lithiation mechanism, which reduce the driving force of cracking. However, due to the low melting point of Sn and Li-Sn alloys, in conjunction with the small particle size promoting fast Li transport, drastic morphological changes occur during delithiation, leading to the generation of smaller NPs, *i.e.*, pulverization (Figure 7b). For the smaller pristine or pulverization-generated NPs with sizes about tens of nanometers (Figure 7c), they can aggregate together during lithiation, forming larger NPs that pulverize upon subsequent cycling. This corresponds to a dynamic process of damaging and/or self-healing. During such process, some small-sized Sn NPs can be isolated from others by the SEI, causing a difficulty in

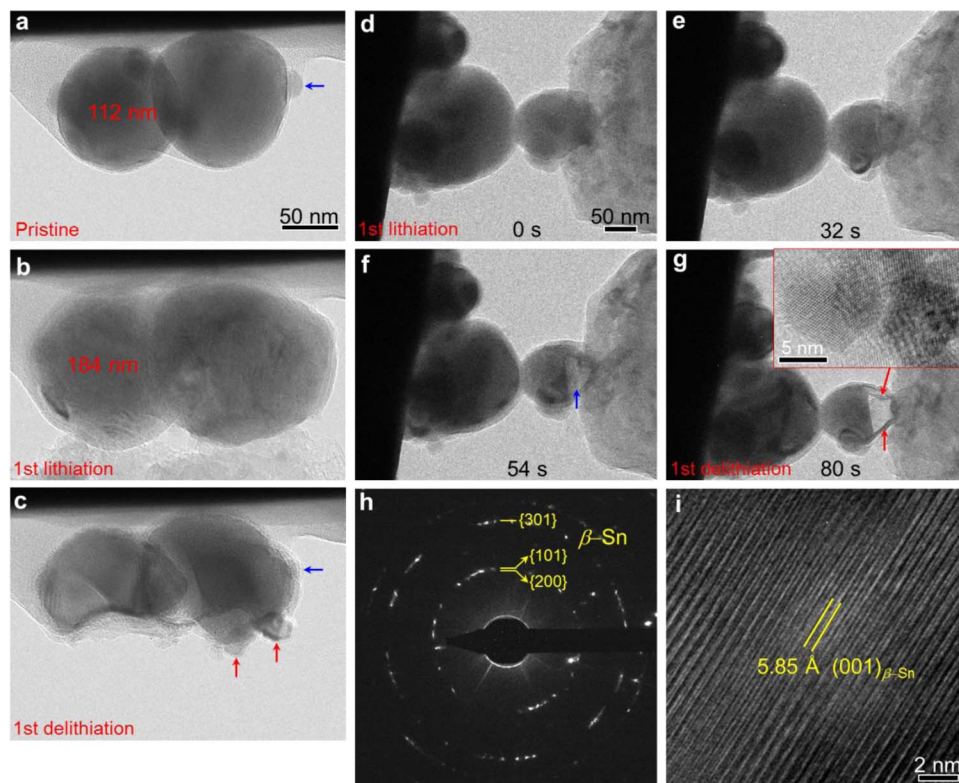


Figure 6. Structural changes of Sn NPs during lithiation-delithiation cycling. (a-c) Morphological evolution of Sn NPs during the first lithiation-delithiation cycle under the beam-blank condition. The spherical pristine NPs become irregular shapes with some smaller NPs generated after delithiation. The blue arrow indicates a pre-existing small Sn NP, while the red arrows point to the newly formed Sn NPs with diameters of ~ 20 nm. (d-g) Delithiation of a NP with a stable surface shell. A surface shell is formed from the lithiated surface oxide layer, serving as the SEI. Upon delithiation, a void forms inside the surface shell. After full delithiation, some small Sn NPs are generated on the surface SEI shell, as indicated by the red arrow and inset in (g). The blue arrow in (f) indicates the void. (h-i) EDP and HRTEM images showing that the NPs are transformed back to β -Sn after full delithiation.

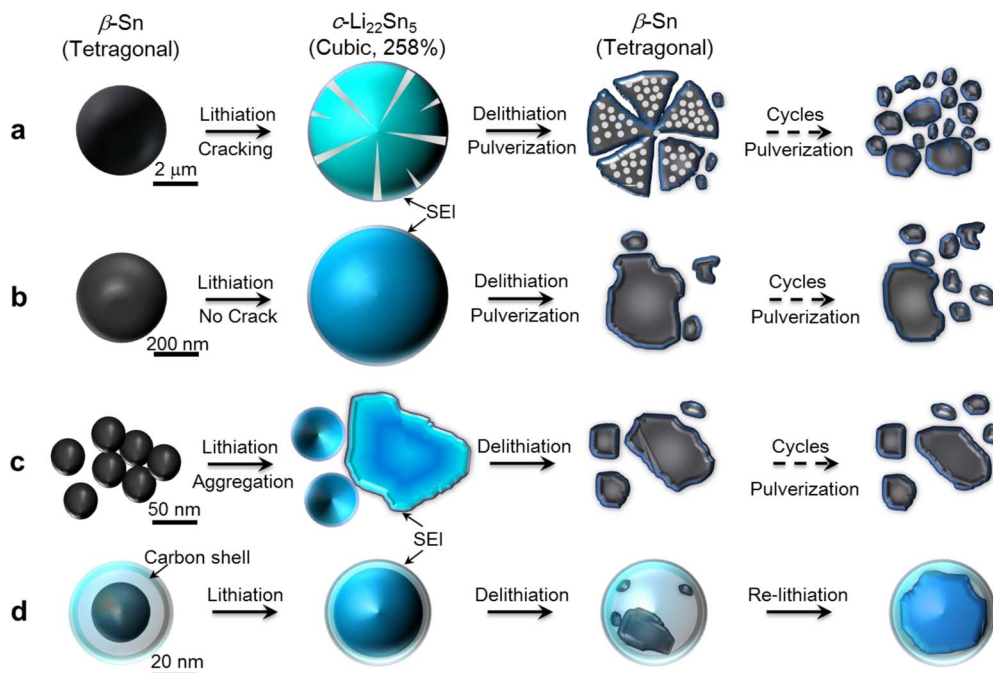


Figure 7. A summary of the size-dependent pulverization mechanisms in Sn particles. (a) In micron-sized Sn particles, the lithiation induces cracking. The SEI grows on fresh new surfaces, so as to prevent the small Sn pieces to be fused together. Pores form after delithiation due to the high rate of Li diffusion. Electrochemical cycling causes the pulverization of Sn particles. (b) In Sn nanoparticles with sizes in hundreds of nanometers, no cracking or fracture occurs after full lithiation, and pulverization is dominated by structural reconstruction during delithiation. (c) In Sn nanoparticles with sizes in tens of nanometers, the lithiation induces aggregation, resulting in larger nanoparticles, which further pulverizes upon cycling. (d) For Sn-C nanocomposites, although the pulverization may generate some small nanoparticles, the electrical contacts are retained in the confined volume of the carbon shell and the nanoparticles can be fused together during cycling, thereby slowing down the capacity fade.

aggregation (Figure 7a–7c). Thus the self-healing capability and the electrode capacity will decay gradually as the cycle number increases. Recently, uniform Sn-C nanocomposites are reported to exhibit excellent electrochemical performance.^{7,11,19} In these nanocomposites, Sn NPs are enclosed by the carbon shell that can serve as a barrier to prevent the aggregation of Sn NPs as well as the SEI formation on the surface of Sn NPs.^{7,11,19} Even if pulverization yields smaller NPs inside the carbon shell, direct contacts between those Sn NPs and Sn/carbon shell could be retained due to the confined volume, such that the pulverized NPs could be effectively fused together in subsequent cycles due to the presence of fresh surface (no SEI formation on the surface of NPs) (Figure 7d). As a result, the pulverization-induced capacity loss can be reduced, thereby enhancing the cyclability.^{7–9,11,12} In this regard, our in situ TEM observation provides a direct evidence that the architecture of Sn NPs embedded in a closed shell would be a favorable design for the Sn-based nanocomposite anode, which could facilitate the retention of a high energy density by mitigating the pulverization during electrochemical cycling. Finally, we note that since Sn particles exhibit similar behaviors during lithiation-delithiation and sodiation-desodiation cycling, the size-dependent pulverization mechanism revealed in this work could hold true in the application of Sn particle anodes in Na-ion batteries.

Conclusions

In conclusion, the structural evolutions of Sn NPs during lithiation-delithiation cycling are studied with in situ TEM. The β -Sn NPs in the size range of 79–526 nm undergo a two-step lithiation, resulting in c -Li₂₂Sn₅ with a total volume expansion of about 258%. No cracking or fracture occurs after full lithiation of Sn NPs, in contrast with the lithiation-induced cracking in micron-sized Sn particles. In addition, lithiation/sodiation can lead to the fusion of small Sn NPs. Delithiation/desodiation causes the pulverization of the relatively large Sn NPs, which can be attributed to the high dealloying rate that induces a large concentration gradient of lithium/sodium and thus a high stress/strain in the dealloyed Sn region. The high stress/strain can induce cracking and facilitate void formation in dealloyed Sn anodes, resulting in smaller Sn particles. Based on the different lithiation-delithiation behaviors of Sn particles, a size-dependent pulverization mechanism is identified. Our results advance the fundamental understanding of the pulverization and degradation mechanisms in Sn-based anodes, which is critical to the design of the mechanically robust Sn-based anodes for high-performance Li-ion batteries. This work also provides a valuable basis for the systematic study of structural evolution and pulverization in Sn-based anodes for Na-ion batteries.

Acknowledgments

T.Z. acknowledges the support by the NSF grants CMMI 1100205 and DMR 1410936. S.X.M. acknowledges the NSF grant CMMI 08010934 through University of Pittsburgh and Sandia National Lab support. This work was performed, in part, at the Center for Integrated Nanotechnologies, a US Department of Energy, Office of Basic Energy Sciences user facility. Sandia National Laboratories is a multiprogram laboratory managed and operated by Sandia Corporation, a wholly owned subsidiary of Lockheed Martin Corporation, for the U.S. Department of Energy's National Nuclear Security Administration under Contract DE-AC04-94AL85000.

References

- M. N. Obrovac, L. Christensen, D. B. Le, and J. R. Dahn, *J. Electrochem. Soc.*, **154**, A849 (2007).
- S. Y. Hong, Y. Kim, Y. Park, A. Choi, N.-S. Choi, and K. T. Lee, *Energy Environ. Sci.*, **6**, 2067 (2013).
- V. Palomares, M. Casas-Cabanas, E. Castillo-Martínez, M. H. Han, and T. Rojo, *Energy Environ. Sci.*, **6**, 2312 (2013).
- M. G. Kim and J. Cho, *Adv. Funct. Mater.*, **19**, 1497 (2009).
- A. R. Kamali and D. J. Fray, *J. Chem. Mater.*, **6**, 156 (2013).
- Y. Xu, Y. Zhu, Y. Liu, and C. Wang, *Adv. Energy Mater.*, **3**, 128 (2013).
- Y. Xu, Q. Liu, Y. Zhu, Y. Liu, A. Langrock, M. R. Zachariah, and C. Wang, *Nano Lett.*, **13**, 470 (2013).
- M. Noh, Y. Kwon, H. Lee, J. Cho, Y. Kim, and M. G. Kim, *Chem. Mater.*, **17**, 1926 (2005).
- G. Derrien, J. Hassoun, S. Panero, and B. Scrosati, *Adv. Mater.*, **19**, 2336 (2007).
- J. Hassoun, G. Derrien, S. Panero, and B. Scrosati, *Adv. Mater.*, **20**, 3169 (2008).
- Y. S. Jung, K. T. Lee, J. H. Ryu, D. Im, and S. M. Oh, *J. Electrochem. Soc.*, **152**, A1452 (2005).
- S. Liang, X. Zhu, P. Lian, W. Yang, and H. Wang, *J. Solid State Chem.*, **184**, 1400 (2011).
- M. G. Kim and J. Cho, *J. Electrochem. Soc.*, **156**, A277 (2009).
- L. Y. Beaulieu, K. W. Eberman, R. L. Turner, L. J. Krause, and J. R. Dahn, *Electrochem. Solid-State Lett.*, **4**, A137 (2001).
- I. A. Courtney, W. McKinnon, and J. Dahn, *J. Electrochem. Soc.*, **146**, 59 (1999).
- H. Li, Q. Wang, L. Shi, L. Chen, and X. Huang, *Chem. Mater.*, **14**, 103 (2001).
- H. Li, L. Shi, W. Lu, X. Huang, and L. Chen, *J. Electrochem. Soc.*, **148**, A915 (2001).
- C. Kim, M. Noh, M. Choi, J. Cho, and B. Park, *Chem. Mater.*, **17**, 3297 (2005).
- Y. Xu, J. Guo, and C. Wang, *J. Mater. Chem.*, **22**, 9562 (2012).
- S.-C. Chao, Y.-F. Song, C.-C. Wang, H.-S. Sheu, H.-C. Wu, and N.-L. Wu, *J. Phys. Chem. C*, **115**, 22040 (2011).
- M. Winter and J. O. Besenhard, *Electrochim. Acta*, **45**, 31 (1999).
- Y.-T. Cheng and M. W. Verbrugge, *J. Electrochem. Soc.*, **157**, A508 (2010).
- K. Afantis and J. Dempsey, *J. Power Sources*, **143**, 203 (2005).
- J. Li, F. Yang, J. Ye, and Y.-T. Cheng, *J. Power Sources*, **196**, 1474 (2011).
- S.-C. Chao, Y.-C. Yen, Y.-F. Song, Y.-M. Chen, H.-C. Wu, and N.-L. Wu, *Electrochem. Commun.*, **12**, 234 (2010).
- J. W. Wang, X. H. Liu, S. X. Mao, and J. Y. Huang, *Nano Lett.*, **12**, 5897 (2012).
- X. H. Liu, J. W. Wang, S. Huang, F. Fan, X. Huang, Y. Liu, S. Krylyuk, J. Yoo, S. A. Dayeh, and A. V. Davydov, *Nat. Nanotechnol.*, **7**, 749 (2012).
- Y. Liu, N. S. Hudak, D. L. Huber, S. J. Limmer, J. P. Sullivan, and J. Y. Huang, *Nano Lett.*, **11**, 4188 (2011).
- J. W. Wang, Y. He, F. Fan, X. H. Liu, S. Xia, Y. Liu, C. T. Harris, H. Li, J. Y. Huang, and S. X. Mao, *Nano Lett.*, **13**, 709 (2013).
- X. H. Liu, L. Zhong, S. Huang, S. X. Mao, T. Zhu, and J. Y. Huang, *ACS Nano*, **6**, 1522 (2012).
- ICSD, *Fachinformationszentrum Karlsruhe*: Karlsruhe, Germany (2006).
- ASM International (The Materials Information Company)*, Volume **3**, 278 (1992).
- L. Xu, C. Kim, A. K. Shukla, A. Dong, T. M. Mattox, D. J. Milliron, and J. Cabana, *Nano Lett.*, **13**, 1800 (2013).
- C. Wang, A. John Appleby, and F. E. Little, *J. Power Sources*, **93**, 174 (2001).
- X. H. Liu, H. Zheng, L. Zhong, S. Huang, K. Karki, L. Q. Zhang, Y. Liu, A. Kushima, W. T. Liang, J. W. Wang, J.-H. Cho, E. Epstein, S. A. Dayeh, S. T. Picraux, T. Zhu, J. Li, J. P. Sullivan, J. Cumings, C. Wang, S. X. Mao, Z. Z. Ye, S. Zhang, and J. Y. Huang, *Nano Lett.*, **11**, 3312 (2011).
- H. Yang, S. Huang, X. Huang, F. F. Fan, W. T. Liang, X. H. Liu, L. Q. Chen, J. Y. Huang, J. Li, T. Zhu, and S. L. Zhang, *Nano Lett.*, **12**, 1953 (2012).
- S. Huang, F. Fan, J. Li, S. L. Zhang, and T. Zhu, *Acta Mater.*, **61**, 4354 (2013).
- W. Liang, H. Yang, F. Fan, Y. Liu, X. H. Liu, J. Y. Huang, T. Zhu, and S. Zhang, *ACS Nano*, **7**, 3427 (2013).
- K. Karki, E. Epstein, J.-H. Cho, Z. Jia, T. Li, S. T. Picraux, C. Wang, and J. Cumings, *Nano Lett.*, **12**, 1392 (2012).
- M. Gu, Y. Li, X. Li, S. Hu, X. Zhang, W. Xu, S. Thevuthasan, D. R. Baer, J.-G. Zhang, and J. Liu, *ACS Nano*, **6**, 8439 (2012).
- X. H. Liu, S. Huang, S. T. Picraux, J. Li, T. Zhu, and J. Y. Huang, *Nano Lett.*, **11**, 3991 (2011).
- Q. Chen and K. Sieradzki, *Nat. Mater.*, **12**, 1102 (2013).
- N. D. Burns, *J. Fail. Anal. Prev.*, **9**, 461 (2009).
- P. M. Le Couteur and B. Jay, *Napoleon's buttons: 17 molecules that changed history*, Penguin, New York (2004).